



## Operating temperature and the responsivity of split-off band detectors

A.G.U. Perera<sup>a,\*</sup>, P.V.V. Jayaweera<sup>a</sup>, S.G. Matsik<sup>a</sup>, H.C. Liu<sup>b</sup>, M. Buchanan<sup>b</sup>, Z.R. Wasilewski<sup>b</sup>

<sup>a</sup> Department of Physics and Astronomy, Georgia State University, Atlanta, GA 30303, USA

<sup>b</sup> Institute for Microstructural Sciences, National Research Council, Ottawa, Ontario, Canada K1A 0R6

### ARTICLE INFO

#### Article history:

Available online 6 June 2009

#### PACS:

71.55.Eq

71.70.-d

71.70.Ej

73.40.Ty

#### Keywords:

Split-off band detector

High operating temperature

### ABSTRACT

A GaAs/AlGaAs heterojunction is used as a spin-split-off band IR detector operating at or around room temperature. This detector structure followed a similar layer architecture to the quantum well IR photo detectors (QWIP) and Heterojunction Interfacial Work function Internal Photoemission (HEIWIP) detectors. Compared to QWIPs, the emitter layer thickness is increased to avoid confinement. Unlike either the QWIPs or HEIWIPs, these detectors will have two energy gaps (barriers) to obtain the wavelength threshold which could be used to design detectors either for optimum operating temperature or optimum responsivity. The free carrier energy gap is determined by the Al fraction and the spin-split-off transition energy provides another handle on controlling the effective threshold of the detector. Unlike QWIPs, these will also detect normal incidence radiation. A preliminary detector showed a peak responsivity of 0.29 mA/W at 2.5  $\mu\text{m}$  at room temperature.

© 2009 Elsevier B.V. All rights reserved.

### 1. Introduction

Uncooled infrared detectors have always attracted much attention due to their numerous applications in data communication, fire fighting, electrical circuit trouble shooting, surveillance, biomolecular identification, astronomy and defense. Avoiding cryogenics for detector cooling can reduce the cost, weight and power requirements: simplifying the sensor systems and allowing for widespread usage. Among military applications, a light weight detector would allow easily portable systems designed for hazard identification and targeting. Operating capability above 300 K indicates the possibility of operation even under extreme conditions, with an allowance for additional heating. One of the major drawbacks of infrared photon detectors is the need for cooling far below room temperature in order to suppress the thermal generation processes. These thermally generated carriers (dark current) effectively reduce the signal to noise ratio of the detector. The cooling requirements introduce difficulties for light weight, portable low power consumption devices. Numerous studies have been conducted over the years to find new material systems and architectures for uncooled IR photon detection [1,2]. An important intrinsic semiconductor material for uncooled infrared photodetector applications [1] has been HgCdTe, which recently showed [3] 200 K operation. Narrow bandwidth quantum well [4] and quantum dot based detectors [5] working at room temperatures have also been reported. Extended InGaAs p–i–n photodiodes responding up to 2.6  $\mu\text{m}$  in ambient conditions are commercially

available. Commercially available 3–5  $\mu\text{m}$  InSb detectors operate at or around 77 K and PbSe detectors operate up to 300 K. However, room temperature detectors have very low quantum efficiencies and are only available in 1D arrays. One of the drawbacks associated with HgCdTe detectors is the difficulties for optimization due to lattice, surface, and interface instabilities. These issues originate from the weak bonding characteristics of II–VI semiconductors and high Hg vapour pressure. Weak bonding reduces the strength of the material, resulting in poor mechanical properties and introduces difficulties in material processing. Moreover, the high Hg vapour pressure makes the composition control over a large area not very practical, causing serious concerns for focal plane array applications. This has intensified the search for alternative infrared material systems and techniques. As a well-developed material system GaAs has an advantage over most other materials.

### 2. Device principles

Highly p-doped GaAs exhibits enhanced absorption in the 2–4  $\mu\text{m}$  range, over the free carrier absorption, due to light hole (L-H)/heavy hole (H-H) to split-off band transitions. The split-off band effects have been experimentally observed in the emission of GaAs metal semiconductor field effect transistors [6] and have enhanced the response of GaInAsP [7] and GaAs [8] quantum wells. Extensive theoretical studies on the importance of the spin-split-off band and the tunneling properties of the holes through  $\text{Al}_x\text{Ga}_{1-x}\text{As}/\text{GaAs}$  heterostructures are reported elsewhere [9]. A split-off band detector [10] responding in the 2–5  $\mu\text{m}$  region at temperatures up to 130 K was demonstrated utilizing a HEIWIP structure designed for the detection of LWIR (threshold 20  $\mu\text{m}$ )

\* Corresponding author. Tel.: +1 404 413 6037; fax: +1 404 413 6025.  
E-mail address: [uperera@gsu.edu](mailto:uperera@gsu.edu) (A.G.U. Perera).

radiation. Absorption results for p-doped GaAs demonstrate that the split-off absorption is much stronger than the free carrier absorption in this range. The increased absorption from the split-off mechanisms on top of the free carrier absorption, combined with the potential for gain in the structures were important motivating factors for the development of the split-off detectors. More recently an uncooled split-off detector was demonstrated responding up to  $5\ \mu\text{m}$  [11]. The split-off band detector is in some ways similar to the HEIWIP detector. The internal work function and hence the free carrier threshold is controlled by the Al fraction. In addition the split-off energy gives a second option of controlling the response by adjusting the free carrier energy barrier. In addition adjusting the group V alloy can vary the split-off energy. This paper describes a set of  $p^+$ -GaAs/ $\text{Al}_x\text{Ga}_{1-x}\text{As}$  heterostructure detectors designed to study the relation between the barrier height and the split-off energy. It was expected that the dark current would decrease as the free carrier threshold is decreased, increasing operating temperature. The collection of the excited carriers from the split-off transition will also depend on the free carrier threshold providing an opportunity for controllability.

As shown in Fig. 1, the detector structure consists of multiple periods of p-doped GaAs emitter and undoped  $\text{Al}_x\text{Ga}_{1-x}\text{As}$  barrier regions sandwiched between two highly doped contact layers. These structures will not form discrete quantum states inside the wells because the emitter layers are doped high enough to have a scattering length similar to the emitter thickness giving a bound

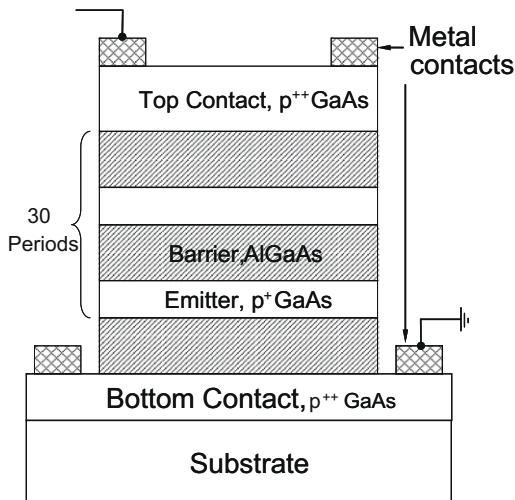


Fig. 1. Schematic of the detector after processing. There were 30 periods consisting of  $3 \times 10^{18}\ \text{cm}^{-3}$  p-doped 188 Å GaAs emitters and 600 Å  $\text{Al}_{0.57}\text{Ga}_{0.43}\text{As}$  barriers.

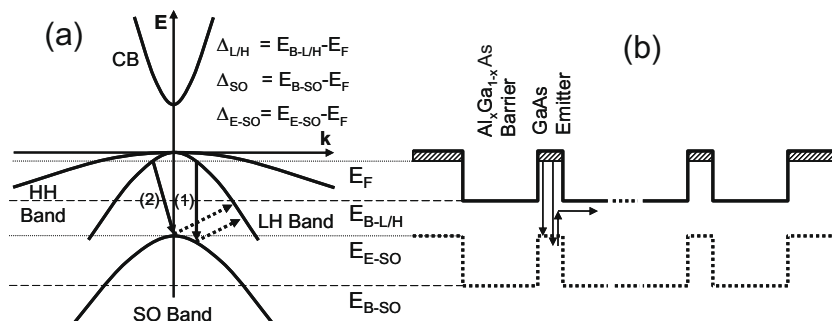


Fig. 2. (a)  $E$ - $k$  diagram for an emitter region of the detector and (b) band diagram of the detector structure illustrating the different IR detection threshold mechanisms. The horizontal dashed lines  $E_{B-L/H}$  and  $E_{B-SO}$  indicate the L-H/H-H and split-off band maximum ( $k=0$ ) positions in the barrier. The horizontal dotted lines  $E_F$  and  $E_{E-SO}$  indicate the Fermi energy and the split-off energy in the emitter at  $k=0$ . The arrows indicate the possible threshold transition mechanisms (1) a direct transition from L-H band to S-O band followed by scattering back to L-H band (2) an indirect transition followed by scattering back to L-H band.

3D carrier distribution in the emitter. An  $E$ - $k$  band diagram for an emitter region of the detector is given in Fig. 2a and the band diagram for the device is shown in Fig. 2b. The L-H and H-H bands which are degenerate at  $k=0$ , and the S-O band which is separated from them by an energy  $E_{E-SO}$ . Under equilibrium conditions, a p-doped region will have a Fermi level between the L-H/H-H and S-O maximum. The detector mechanism consists of three main steps: (I) photo-absorption exciting the carriers from the emitters, (II) escape of the photo excited carriers and (III) the sweep out and collection of the escaped carriers. The possible thresholds for the direct and indirect transitions indicated by the arrows in the Fig. 2. Carrier in the S-O band, can escape directly or scatter back into the L-H/H-H bands and then escape. A direct transition (shown by arrow 1 solid part) will conserve  $k$  as no phonon is involved. The excited carrier then must scatter back to the L-H/H-H bands before escaping as shown by the dashed arrow. The direct transition threshold energy is the difference of the light and S-O hole energies at  $k$  corresponding to the Fermi energy shown by  $E_F$  in the Fig. 2. For the indirect transition (shown by arrow 2) involving a phonon there are two threshold energies depending on the escape mechanism. The high energy transition which is below the barrier in the S-O band could escape directly as for excited free carriers in HEIWIPs.

The threshold energy for this case is the difference between the Fermi energy and the S-O band at  $k=0$  in the barrier ( $\Delta_{SO}$ ). Indirect transition above a threshold energy equal to the difference of the Fermi energy and the S-O band at  $k=0$  in the emitter ( $\Delta_{E-SO}$ ) can escape after scattering into the L-H/H-H as for the direct transition shown in Fig. 2. The horizontal dashed lines labeled  $E_{B-L/H}$  and  $E_{B-SO}$  indicate the L-H/H-H and S-O band maximum (at  $k=0$ ) level in the  $\text{Al}_x\text{Ga}_{1-x}\text{As}$  barrier. The horizontal dotted lines  $E_F$  and  $E_{E-SO}$  indicate the Fermi energy and the S-O energy at  $k=0$ . The lowest barrier for the excited carriers in L-H/H-H bands is  $\Delta_{L/H}$  which determines the threshold wavelength for free carrier response and thermionic dark current hence controlling maximum operating temperature. Increasing  $\Delta_{L/H}$  can also reduce escape probability and gain. The optimum value will be determined by the key application requirement high operating temperature or high performance.

### 3. Technology

Three detector structures with different Al fractions  $x = 0.28, 0.37, 0.57$  (with corresponding  $\Delta_{L/H}$  values 55, 207, 310 meV and threshold wavelengths 8, 6, 4  $\mu\text{m}$ ) were grown on semi insulating GaAs substrates. The structure contains a 0.7  $\mu\text{m}$  thick bottom contact layer, of  $1 \times 10^{19}\ \text{cm}^{-3}$  p-doped GaAs followed by 30 periods

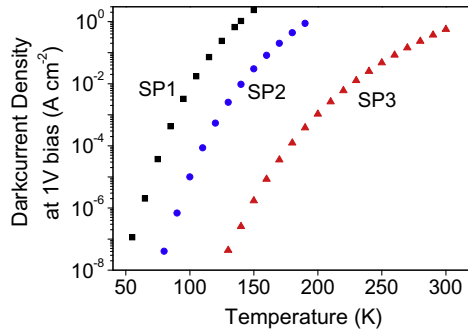


**Fig. 3.** The dark current density vs. temperature for samples SP1, SP2, and SP3 under 1 V applied bias. The samples SP1, SP2, and SP3 have barriers with Aluminum fractions 0.28, 0.37, and 0.57, respectively. The dark current densities reached  $\sim 1$  A/cm<sup>2</sup> for each sample at 140, 190, and 300 K. The experimentally observed, operating temperatures for each sample.

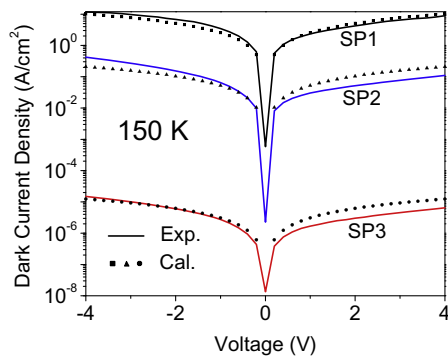


**Fig. 4.** The dark current density for the three samples measured at 150 K showing thermionic emission. SP2 shows factor of 70 higher current than SP1. SP3 sample dark current was six orders of magnitude higher than SP1.

of a 600 Å undoped Al<sub>x</sub>Ga<sub>1-x</sub>As barrier and  $3 \times 10^{18}$  cm<sup>-3</sup> p-doped 188 Å GaAs emitter. The last emitter was 0.2 μm thick and p-doped to  $1 \times 10^{19}$  cm<sup>-3</sup> in order to serve as the top contact layer. The detectors were processed by wet etching to form square mesas with sides 400, 600, 800, and 1000 μm. Ti/Pt/Au ohmic contacts were evaporated onto the top and bottom contact layers. A ring contact was used on the top surface and a window was opened through the top contact for front side illumination. A schematic of a single mesa of the detector is shown in Fig. 1. The current voltage (*I*-*V*) characteristics were measured with different temperatures from 70 to 300 K. As shown in Fig. 3, dark current density at 1 V bias reached the same order at 140, 190 and 300 K for samples SP1, SP2, and SP3, respectively. The measured dark current densities of SP1, SP2, and SP3 at 150 K temperatures (solid lines) are consistent with a thermionic model (dots) as shown in Fig. 4. A comparison of the measured dark current density for the three samples at 1 V bias and 150 K is presented in Table 1. The sample

SP3 with 310 meV barrier has a dark current six orders of magnitude lower than the sample SP1 which has a 155 meV barrier. The experimental results showed that the highest operating temperature (330 K) detector sample was the lowest threshold sample  $\lambda_0 = 4$  μm sample (SP3).

**4. Device performance**

The spectral response of the detectors SP1, SP2, and SP3 were measured using a Fourier transform infrared spectrometer (Perkin-Elmer system 2000) at temperatures up to 140, 190, and 300 K, respectively. Responsivity calibrated using a bolometer and also a calibrated InGaAs photo diode at 2.5 μm. A response model based on photoexcitation and scattering between the hole bands has been developed to predict the escape efficiency and the gain of the detector. The modeling calculations were done using an eight band *k.p* approach [12]. The scattering length for hot and cold carriers was determined by fitting the response for SP3, SP2, and SP1 with free carrier thresholds of 4, 6, and 8 μm giving a scattering length of  $\sim 80$  nm which is similar to the mean distance between the cold carriers of 75 nm calculated from the doping density in the emitters. The full response with the free carrier threshold (zero response) can be seen in Fig. 5 where the responsivity is given for all three detectors at 4 V bias and a temperature of 80 K. The peak responsivity (at 2.6 μm) of sample SP2 was a factor of three higher than sample SP3. However, the peak responsivity of sample SP1 was more than 400 times the SP2 peak response. The large difference between the SP1 and SP2 samples could be due to the large increase in gain due to impact ionization when the barrier is decreased from 207 to 155 meV in compares with the split-off energy 365 meV. By adjusting the free carrier threshold energy, the maximum operating temperature and the peak response can be adjusted, indicating that the detector design can take the operating temperature and responsivity requirements into account as needed. The measured and calculated responsivity of SP3 at 300 K under four different biases is shown in Fig. 6, with a reasonable agreement. The predicted peak response is within  $\sim 20\%$  of the measured peak value for all the biases as seen in Fig. 7 for the sample with a 4 μm threshold. The deviation seen at long wavelengths beyond  $\sim 3.5$  μm appears to be due to a thermal detection mode that is also present which is not included in the modeling. Inclusion of this mechanism would improve the fit at wavelengths longer than the free carrier threshold. This model was also tested with SP1 and SP2 results and gave similar results.

Normalized detectivity ( $D^*$ ) was calculated using the measured noise current density with the sample mounted in an optically and electrically shielded dewar. The primary noise sources are believed to be the generation recombination and Johnson noise.  $D^*$  was obtained using the formula  $D^* = (R \times \sqrt{A})/I_N$ , where *R* is the responsivity (in A W<sup>-1</sup>), *A* is the optically active area of the detector (in cm<sup>2</sup>) and *I<sub>N</sub>* is the noise current density (in A Hz<sup>-1/2</sup>). The calculated responsivity and  $D^*$  values for each sample operating at 150 K temperature is listed in Table 1.  $D^*$  of the SP3 sample at room temperature was  $6.8 \times 10^5$  Jones. Preliminary indications are such that the

**Table 1**

Sample parameters at 150 K temperatures. The dark current density (*I<sub>dark</sub>*) at 1 V bias, and peak responsivity and  $D^*$  at 2.6 μm were experimentally measured.  $\Delta_{L/H}$  and  $\lambda_t$  are the designed band offset and corresponding threshold wavelength.

Sample	$\Delta_{L/H}$ (meV)	$\lambda_t$ (μm)	150 K		
			1 V bias		4 V bias at 2.6 μm
			Dark current (A/cm <sup>2</sup> )	Responsivity (mA/W)	$D^*$ (Jones)
SP1	155	8	$2.34 \times 10^0$	$2.3 \pm 0.1$	$(2.1 \pm 0.1) \times 10^6$
SP2	207	6	$3.01 \times 10^{-2}$	$0.96 \pm 0.01$	$(2.0 \pm 0.1) \times 10^7$
SP3	310	4	$1.72 \times 10^{-6}$	$(2.1 \pm 0.1) \times 10^{-3}$	$(2.2 \pm 0.1) \times 10^{10}$

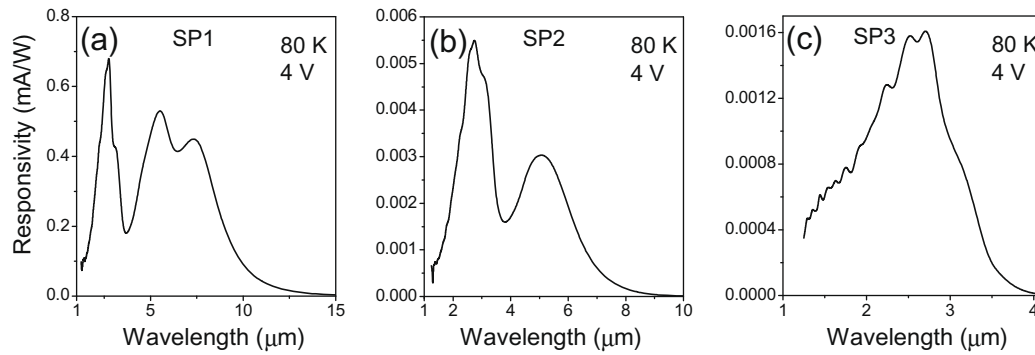


**Fig. 5.** The response at 80 K for 4 V bias measured for all three samples. The SP2 detector response is thrice for the SP3 sample, and SP1 detector response was 400 times that for the SP2 detector. As the free carrier threshold is increased, the responsivity increases but the maximum operating temperature is lowered. Hence the peak responsivity and the highest operating temperature will inversely depend on each other. The SP1 and SP2 samples clearly shows the split-off and free carrier peaks with 13 and 9  $\mu\text{m}$  free carrier thresholds. Sample SP3 with free carrier threshold 4  $\mu\text{m}$  shows only the split-off response.

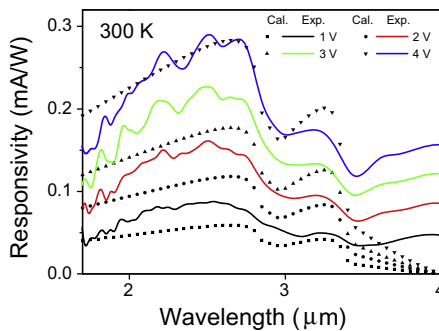


**Fig. 6.** The measured spectra and the calculated response for the detector under 1, 2, 3, and 4 V biases at 300 K showing peaks around 2.7  $\mu\text{m}$ . The deviation at long wavelengths is due to the thermal mechanism which is not included in the model.

room temperature SP3 response appears to be due to a single emitter with other emitters not contributing. As shown in Fig. 6 the responsivity increases with the bias up to 4 V, but increased dark current (low dynamic resistance) reduced the response above a 4 V bias. The threshold wavelengths for the response mechanisms 1 and 2 shown in Fig. 2a can be identified in Fig. 6 at 2.9  $\mu\text{m}$  and 3.4  $\mu\text{m}$ , respectively. At 300 K mechanism (1) becomes dominant, as can be seen by the much larger step at 2.9  $\mu\text{m}$ . The threshold for the free carrier response increased slowly with temperature due to the increased number of carriers above the Fermi energy, which can give response at longer wavelengths. The SP1 and SP2 detectors had maximum operating temperatures of 140 and 190 K, respectively. The higher responsivity and  $D^*$  was seen for longer wavelength threshold samples possibly due to impact ionization (gain), compared to the shorter threshold samples. In order to increase the uncooled response of the split-off detectors, the gain must be increased. The limiting factor on gain in the present design is the trapping due to scattering between hot and cold carriers as the holes pass through the emitter layers. For a detector with a free carrier threshold near 4  $\mu\text{m}$ , nearly 100% of the carriers will be trapped and then reemitted at the barrier. This effectively limits the gain for the detector to  $1/N$ , where  $N$  is the number of emitter periods. Initial model calculations suggested that a single emitter device with graded barrier on one side of the emitter and double barrier structure on the other side of the emitter will be the optimum design to obtain the maximum gain. By tailoring the shape of the initial barrier it is possible to produce a significant increase in the space charge of the emitter under illumination. This will lead to a photocurrent gain which is larger than for the dark current gain.

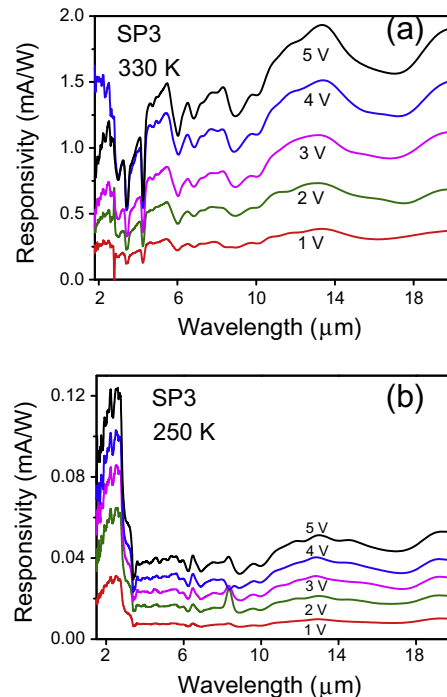


**Fig. 7.** The responsivity of the split-off detector SP3 in the 2–20  $\mu\text{m}$  range for different bias values in the 1–5 V range. (a) At 330 K temperature, the maximum long wavelength response was  $\sim 1.9$  mA/W for a bias of 5 V. Peak responsivity of the split-off range was  $\sim 1.2$  mA/W at same bias. (b) At 250 K temperature the maximum long wavelength response was  $\sim 0.05$  mA/W and split-off responsivity was 0.12 mA/W for a bias of 5 V. The response was nearly constant over most of the range.

In addition to the expected split-off response in 2–4  $\mu\text{m}$  range, a long wavelength response was also observed for the detector SP3. The responsivity in the 2–20  $\mu\text{m}$  range for various bias voltages at a temperature of 250 and 330 K are shown in Fig. 7a and b, respectively. This response extends to much longer wavelengths than the free carrier response threshold of 4  $\mu\text{m}$ . When the incident radiation was blocked, no signal was observed. The current responsivity (A/W) increases with increase operating temperature as seen in Fig. 7a and b. The ratio of the long wave response ( $R_{lw}$ ) to split-off response ( $R_{sp}$ ) was increased with the temperature ( $R_{lw}/R_{sp} = 0.4$  at 250 K and  $R_{lw}/R_{sp} = 1.6$  at 330 K) showing that long wavelength response mechanism is dominant at higher temperatures. This indicates that the response is probably associated with

changes in the thermal population of the carriers at higher temperatures. A possible explanation is that the response originates with the excited carriers in the split-off band, which is 340 meV above the light/heavy hole bands. Unlike the standard semiconductor bolometric response in which the signal is due to the increased number of electrons and holes produced through thermal generation, the signal in this detector comes from an increase in the number of carriers in the split-off band at higher temperatures. The carriers in the split-off band could then scatter into the light/heavy hole bands above the barrier and escape. The escaped carriers would then be collected by an applied electric field, contributing to the photocurrent.

The larger doping used to obtain a high absorption in the GaAs/AlGaAs based split-off detectors has shifted the peak of the split-off absorption to below 3  $\mu\text{m}$  for process (1) which is the dominant response mechanism at higher temperatures. By reducing the doping, the split-off response peak can be moved to near 3.5  $\mu\text{m}$  but the response will be reduced. Hence, the use of alternate materials would be the best option. For extending the wavelength range for 3–5 and 8–14 atmospheric windows Arsenide and phosphide would be the best materials since their split-off energies fall in this range. A bandgap vs. lattice constant plot of selected arsenide and phosphide materials is shown in Fig. 8. By using GaAsP as the emitter, the split-off threshold ( $\lambda_s$ ) could be tailored. An emitter with GaAs<sub>0.4</sub>P<sub>0.6</sub> should give a split-off threshold near 5  $\mu\text{m}$ , allowing full coverage of the 3–5  $\mu\text{m}$  range. However, there would be significant strain between the emitters and barriers in a structure that only used GaAsP emitters and AlGaAs barriers. The strain associated with the high P fraction would introduce defects, reducing the material quality. As shown in Fig. 8, well matched lattice constants of GaP and AlP (5.4505 and 5.4510 Å [13]) will allow an Al<sub>x</sub>Ga<sub>1-x</sub>P ternary alloy and GaP to be latticed matched for all  $x$  values from 0 to 1. Heterojunction devices with a  $p$ -GaP emitter and an Al<sub>x</sub>Ga<sub>1-x</sub>P barrier on a GaP substrate should behave similarly to the well known  $p$ -GaAs/AlGaAs system. The free carrier threshold of the  $p$ -GaP/Al<sub>x</sub>Ga<sub>1-x</sub>P system can be tuned to GaP split-off energy of 80 meV (16  $\mu\text{m}$ ) by changing Al fraction  $x$  but still keeping lattice matched conditions. Growth of these structures should not be difficult since characteristics of GaP/AlGaP heterojunctions [14], superlattice [15], heterostructure based detectors, [16] and solar cells [17] have already been reported.

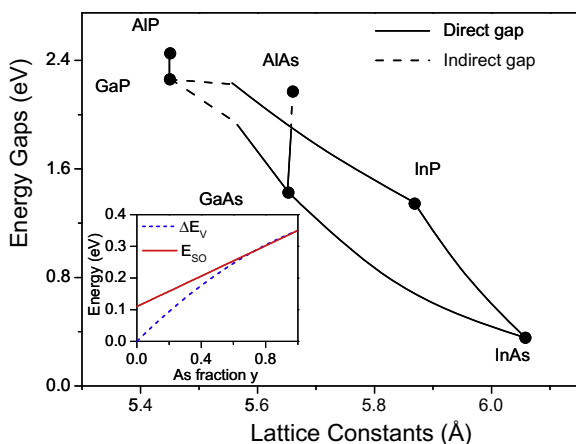


**Fig. 8.** Band gap and lattice constant of selected III-V semiconductors (data were taken from “Handbook series on semiconductor parameters [13]”). Solid lines represent direct band region and dashed lines represent indirect band region. GaP/AlGaP would be a high-quality, lattice matched system similar to GaAs/AlGaAs. Also, InGaAs and InGaP can be lattice matched to InP and GaAs, respectively. The inset shows the variation of the valence band offset energy ( $\Delta E_V$ ) and split-off energy ( $E_{S0}$ ) of the  $\text{In}_{1-x}\text{Ga}_x\text{As}_y\text{P}_{1-y}/\text{InP}$  heterostructure with Arsenic fraction  $y$ . To achieve  $\Delta E_V$  similar to  $E_{S0}$ , the Arsenic fraction should be in the 0.5–0.7 range.

Processing of these devices will also be straight forward since different etching methods for GaP/AlGaP have also been developed [18].

Another possible material system would be  $\text{In}_{1-x}\text{Ga}_x\text{As}_y\text{P}_{1-y}$  that can be lattice matched to InP when  $x = 0.47y$ . The split-off energy of  $\text{In}_{1-x}\text{Ga}_x\text{As}_y\text{P}_{1-y}$  can be tuned for a wide energy range from 0.11 to 0.379 eV (3.3–11  $\mu\text{m}$ ) by changing the As alloy fraction  $y$  from 0 to 1 ( $E_{S0} = 0.11 + 0.24y$ ) [19]. Hence, a detector with  $p$ -InGaAsP emitter and InP barrier would be a potential choice for a tunable split-off threshold from  $\sim 3$  to 11  $\mu\text{m}$ . Since the valence band discontinuity of the  $\text{In}_{1-x}\text{Ga}_x\text{As}_y\text{P}_{1-y}/\text{InP}$  heterostructure can be expressed as [13]  $\Delta E_V = 0.502y - 0.152y^2$ , the free carrier threshold wavelength will also be tunable. In order to achieve  $\Delta E_V$  similar to  $E_{S0}$ , “ $y$ ” should be within 0.5–0.7 range. This corresponds to a threshold wavelength in the 4–5  $\mu\text{m}$  range. A calculated  $\Delta E_V$  and  $E_{S0}$  for different Arsenic fractions  $y$  is shown in the inset of Fig. 8. It is possible to grow InGaAsP with the In and P fractions chosen so that structure would be lattice matched to GaAs. The barrier can also be tailored using AlGaAs. A device with  $\text{In}_{0.3}\text{Ga}_{0.7}\text{As}_{0.4}\text{P}_{0.6}$  would be lattice matched to GaAs and would have a split-off threshold of 5.1  $\mu\text{m}$  for process (1), which is the dominant split-off mechanism. The barriers in an optimized detector would be  $\text{Al}_{0.30}\text{Ga}_{0.70}\text{As}$ . Thus the device structure would consist of  $3 \times 10^{18} \text{ cm}^{-3}$  doped, 200 Å  $\text{In}_{0.3}\text{Ga}_{0.7}\text{As}_{0.4}\text{P}_{0.6}$  emitters and 400 Å  $\text{Al}_{0.30}\text{Ga}_{0.70}\text{As}$  barriers.

## 5. Conclusions

A set of infrared detector based on a GaAs/AlGaAs multiple heterostructures were reported. The response is primarily from heavy/light hole to split-off transitions, and the detector showed a peak  $D^*$  of  $6.8 \times 10^5$  Jones at 2.5  $\mu\text{m}$  300 K. As a well-developed material system, (III)–(V) system GaAs is a feasible solution to future uncooled infrared detection; hence high-quality growth and integration with other readout electronics is readily available. Materials other than GaAs/AlGaAs may help to extend the coverage to longer wavelengths. Possible materials such as phosphides (with a threshold of  $\sim 18 \mu\text{m}$ ) and nitrides may be able to operate at 60  $\mu\text{m}$  or beyond at elevated temperatures. A possible dual-band detector design could cover 3–5  $\mu\text{m}$  and 8–14  $\mu\text{m}$  atmospheric windows using a combined system with arsenides and phosphides. The response can be optimized by using a graded-heating-barrier that reduces trapping and increases the gain. A properly optimized device working at room temperature may compete with currently available uncooled detectors [20,21].

## Acknowledgements

This work is supported by US Army under Grant No. W911NF-08-1-0448. Authors acknowledge fruitful discussions with Dr. P. Wijewarnasuriya and K.K. Choi at US Army.

## Reference

- [1] J. Piotrowski, A. Rogalski, *Infrared Physics & Technology* 46 (2004) 115–131.
- [2] M.R. Watts, M.J. Shaw, G.N. Nielson, *Nature Photonics* 1 (2007) 632–634.
- [3] N.T. Gordon, D.J. Lees, G. Bowen, T.S. Phillips, M. Haigh, C.L. Jones, C.D. Maxey, L. Hipwood, R.A. Catchpole, *Journal of Electronic Materials* 35 (2006) 1140–1144.
- [4] H. Alause, W. Knap, J.L. Robert, R. Planel, V. Thierry-Mieg, F.H. Julien, K. Zekentes, V. Mosser, *Semiconductor Science and Technology* 15 (2000) 724–727.
- [5] G. Ariyawansa, A.G.U. Perera, X.H. Su, S. Chakrabarti, P. Bhattacharya, *Infrared Physics & Technology* 50 (2007) 156–161.
- [6] K.S. Zhuravlev, V.A. Kolosov, A.G. Milekhin, V.G. Polovinkin, T.S. Shamirzaev, Yu N. Rakov, Yu B. Myakishev, J. Fryar, E. McGlynn, M.O. Henry, *Semiconductor Science and Technology* 19 (2004) S94–S95.
- [7] J.R. Hoff, M. Razeghi, G.J. Brown, *Physical Review B* 54 (1996) 10773–10783.

- [8] B.W. Kim, E. Mao, A. Majerfeld, *Journal of Applied Physics* 81 (1997) 1883–1889.
- [9] S. Ekbote, M. Cahay, K. Roenker, *Physical Review B* 58 (1998) 16315.
- [10] A.G.U. Perera, S.G. Matsik, P.V.V. Jayaweera, K. Tennakone, H.C. Liu, M. Buchanan, G. Von Winckel, A. Stintz, S. Krishna, *Applied Physics Letters* 89 (2006). 131118–3.
- [11] P.V.V. Jayaweera, S.G. Matsik, A.G.U. Perera, H.C. Liu, M. Buchanan, Z.R. Wasilewski, *Applied Physics Letters* 93 (2008). 021105–3.
- [12] E.O. Kane in: R.K. Willardson, C. Albert (Eds.), *Semiconductors and Semimetals*, vol. 1, Beer Academic Press, New York, 1966, pp. 75–100.
- [13] M.E. Levinshtein, S.L. Rumyantsev, M. Shur, *Handbook Series on Semiconductor Parameters*, World Scientific, Singapore, New Jersey, 1996.
- [14] K. Adomi, N. Noto, A. Nakamura, T. Takenaka, *Journal of Crystal Growth* 124 (1992) 570.
- [15] Y. Nabetani, A. Wakahara, A. Sasaki, *Materials Science and Engineering–Lausanne – B* 35 (1995) 454–458.
- [16] T.A. Prutsikij, V.M. Andreev, V.R. Larionov, *Solar Energy Materials and Solar Cells* 37 (1995) 349–355.
- [17] O.V. Sulima, P.E. Sims, J.A. Cox, M.G. Mauk, R.L. Mueller, R.C. Reedy, Jr., A.M. Khammadov, P.D. Paulson, G.A. Landis, in: *High-Temperature AlGaP/GaP Solar Cells for NASA Space Missions*, vol. 1, 2003, pp. 737–740.
- [18] J.H. Epple, C. Sanchez, T. Chung, K.Y. Cheng, K.C. Hsieh, *Journal of Vacuum Science and Technology B Microelectronics and Nanometer Structures* 20 (2002) 2252–2255.
- [19] Y. Yamazoe, T. Nishino, Y. Hamakawa, *IEEE Journal of Quantum Electronics* 17 (1981) 139–144.
- [20] A. Rogalski, *Opto-Electronics Review* 12 (2004) 221–245.
- [21] M.Z. Tidrow, W.W. Clark Iii, W. Tipton, R. Hoffman, W.A. Beck, S.C. Tidrow, D.N. Robertson, H.K. Pollehn, K.R. Udayakumar, H.R. Beratan, K.L. Soch, C.M. Hanson, M. Wigdor, in: *Uncooled Infrared Detectors and Focal Plane Arrays*, Beijing, China, (SPIE), 1998. pp. 178–187.